Structural, elastic, electronic, magnetic, optical, and thermoelectric properties of the diamond-like quaternary semiconductor $CuMn_2InSe_4$

L. Salik, A. Bouhemadou, K. Boudiaf,
F. Saad Saoud, S. Bin-Omran,
R. Khenata, Y. Al-Douri & A. H. Reshak

ONLINE FIRST

Journal of Superconductivity and Novel Magnetism

Springer

Springer

Springer

ORIGINAL PAPER

Structural, elastic, electronic, magnetic, optical, and thermoelectric properties of the diamond-like quaternary semiconductor CuMn$_2$InSe$_4$

L. Salik[1] · A. Bouhemadou[2] · K. Boudiaf[2] · F. Saad Saoud[1] · S. Bin-Omran[3] · R. Khenata[4] · Y. Al-Douri[5,6,7] · A. H. Reshak[8,9,10]

Abstract

A theoretical study of the structural, elastic, electronic, optical, magnetic, and thermoelectric properties of the newly synthetized diamond-like quaternary semiconductor CuMn$_2$InSe$_4$ was carried out in this paper. The calculated equilibrium structural parameters are in excellent agreement with available experimental data. The single-crystal and polycrystalline elastic moduli were predicted using energy strain technique. Electronic properties, including band energy dispersion, total and projected densities of states, and charge distribution map, were calculated and analyzed. Total and local magnetic moments were determined. Linear optical functions were predicted from the calculated band structure. We studied the chemical potential dependence of the thermoelectric parameters, including Seebeck coefficient, electrical conductivity, thermal conductivity, and power factor. The maximum power factor and the corresponding chemical potential are estimated. The obtained results were compared with available ones.

Keyword Diamond-like quaternary semiconductors · First-principles calculations · Electronic structure · Optical functions · Thermoelectric coefficients · Elastic constants

1 Introduction

Diamond-like quaternary semiconductors (DLQSs), with a great variety of possible compositions (large variety of constituent atoms), crystalline structures, and physical characteristics, are promising materials for wide technological applications in some different fields, such as thermoelectrics [1–4], tunable semiconductors [5–9], spintronics [10], photovoltaics and solar cells [11–15], and non-linear optics [16–18]. Diamond-like quaternary semiconductors with the chemical

✉ A. Bouhemadou
abdelmadjid_bouhemadou@univ-setif.dz;
a_bouhemadou@yahoo.fr

1 Laboratory of Physics of Materials, Radiations and Nanostructures (LPMRN), Department of Science and Technique, Faculty of Sciences and Technology, University Mohamed El Bachir Ibrahimi, 34000 Bordj Bou-Arreridj, Algeria

2 Laboratory for Developing New Materials and their Characterizations, Department of Physics, Faculty of Science, University Ferhat Abbas Setif 1, 19000 Setif, Algeria

3 Department of Physics and Astronomy, College of Science, King Saud University, Riyadh, Saudi Arabia

4 Laboratoire de Physique Quantique de la Matière et de Modélisation Mathématique (LPQ3M), Université de Mascara, 29000 Mascara, Algeria

5 University Research Center, Cihan University Sulaimaniya, Sulaimaniya 46002, Iraq

6 Nanotechnology and Catalysis Research Center (NANOCAT), University of Malaya, 50603 Kuala Lumpur, Malaysia

7 Department of Mechatronics Engineering, Faculty of Engineering and Natural Sciences, Bahcesehir University, 34349, Besiktas, Istanbul, Turkey

8 Department of Instrumentation and Control Engineering, CTU in Prague, Technicka 4, 166 07 Prague 6, Czech Republic

9 Nanotechnology and Catalysis Research Center (NANOCAT), University of Malaya, 50603 Kuala Lumpur, Malaysia

10 Iraq University College (IUC), Al-Estiqlal St, Basrah, Iraq

formula I-II$_2$-III-VI$_4$, where I = Cu, Ag; II = Zn, Cd, Mn, Fe; III = Al, Ga, In; and VI = S, Se, Te, which are derived from the II-VI cubic zincblende structure ($F\overline{4}3m$ symmetry group) by substituting the divalent group II cation with two or three different kinds of cations, are an attractive group of materials belonging to the DLQS family. Recently, Delgado and Sagredo [19] synthesized the CuMn$_2$InSe$_4$ compound, a new magnetic semiconductor member of the I-II$_2$-III-VI$_4$ family, which was structurally characterized by single-crystal X-ray diffraction analysis. This compound crystalizes in the tetragonal space group 142m [19]. Magnetic semiconductors are of great interest because of their peculiar magnetic and magneto-optical properties arising from the presence of magnetic ions in the lattice [20]. Apart from its elaboration and crystalline structure characterization, experimental data for CuMn$_2$InSe$_4$ are scarce. On the theoretical side, the electronic and magnetic properties of the CuMn$_2$InSe$_4$ compound have been studied by Berri [21] using the full-potential linearized augmented plane wave (FP-LAPW) method with the Perdew-Burke-Ernzerhof form of the generalized gradient approximation (GGA-PBE) [22], and by Han et al. [23] using the pseudopotential plane wave (PP-PW) method with the GGA-PBE approach. A more accurate functional to model the exchange–correlation potential for better description of the electronic structure of this compound is required because the common GGA is known by its underestimation of the band gap. For this purpose, we used the full-potential augmented plane wave plus local orbitals (FP-APW + lo) method with Tran–Blaha modified Becke–Johnson (TB-mBJ) potential [24,25], which has been shown to give very much improved band gaps than other semilocal functionals for a large variety of semiconductors and insulators [26–29], to re-examine with more details the electronic and magnetic properties of CuMn$_2$InSe$_4$ and to conduct a theoretical investigation of its elastic, optical, and transport properties for the first time to shed some light on its performance for eventual application in the optoelectronic and thermoelectric conversion devices.

The paper is organized as follows. Section 2 is devoted to a brief description of the computational techniques. The obtained results are presented, analyzed, and discussed in Section 3. The main conclusions are gathered in Section 4.

2 Computational Details

All our first-principles calculations were executed by employing the full-potential linearized augmented plane wave plus local orbitals (FP-LAPW + lo) method in the framework of density functional theory (DFT) as rooted in the WIEN2k package [30]. To calculate the structural properties, the local-density approximation (LDA) [31] and generalized gradient approximation of Perdew et al. [32] (the so-called GGA-PBEsol) were employed to model the exchange–correlation energy. Generally, the common GGA and LDA functionals underestimate the band gap values of semiconductors and insulators when compared with the corresponding measured ones. To overcome the major problem of underestimation of the band gap, some functionals upon the GGA and LDA have been developed for a better description of the electronic structures of semiconductors and insulators. Among these functionals, Tran–Blaha modified Becke–Johnson potential (TB-mBJ) [25] yields accurate band gap values for a large class of semiconductors and isolators [26–29]. Predicted band gap values through the TB-mBJ approach are practically comparable with the experimental ones with much less computing time when compared with the HSE (screened hybrid functional) and GW (Green's function G and screened Coulomb interaction W) methods. Therefore, the electronic, magnetic, optical, and thermoelectric properties of the examined system were studied through the TB-mBJ functional in order to provide electronic structure data more accurate than those previously reported [21, 23]. The wave functions in the interstitial region were expanded on a plane wave basis set with a cutoff parameter $R_{MT}^{\min}K_{\max} = 9$, where $K_{\max}$ is the cutoff for the wave function and $R_{MT}^{\min}$ is the smallest radii of the muffin-tin spheres. The muffin-tin sphere radius R_{MT} was chosen to be equal to 2.32 au for Cu, 2.42 au for Mn, 2.50 au for In, and 2.2 au for Se. The structural properties were calculated using a 10 × 10 × 10 Monkhorst–Pack k-mesh, whereas the electronic, magnetic, optical, and thermoelectric properties were obtained by using a 30 × 30 × 30 Monkhorst–Pack k-points grid. All atomic positions of the examined compound were relaxed until all forces became smaller than 0.5 mRy (au)$^{-1}$. The self-consistent calculations were iterated until the total energy converges below 10^{-5} Ry. Thermoelectric coefficients were calculated through first-principles calculations and solving Boltzmann transport equations in conjunction with the rigid band and constant relaxation time (τ) approximations as implemented in the BoltzTraP code [33].

3 Results and Discussion

3.1 Structural Properties

The diamond-like quaternary semiconductor CuMn$_2$InSe$_4$ crystallizes stably in the tetragonal stannite structure with space group $I\overline{4}2m$ (no. 121) [19]. There are 2 copper, 4 manganese, 2 indium, and 8 selenium atoms in the conventional unit cell at 2a (0, 0, 0), 4d (0, 0.5, 0.25), 2b (0, 0, 0.5), and 8i (x_{Se}, $y_{Se} = x_{Se}$, z_{Se}) Wyckoff positions, respectively. This structure can be regarded as a double-periodic cubic zincblende supercell in the z-direction, in which Zn is orderly substituted

by three different types of metal cations. Similar to the zincblende lattice, each metal cation is coordinated by four nearest neighbor anions, forming a tetrahedrally bonded structure [5]. The conventional unit cell of the $CuMn_2InSe_4$ compound is depicted in Fig. 1. As first step, the equilibrium structural parameters were calculated by minimizing the total energy via a full relaxation of the experimental structure [30]. Experimental parameters of $CuMn_2InSe_4$ from [19] were used as initial input data to perform our calculations. The computed equilibrium conventional unit cell parameters (a and c), internal atomic coordinates (x_{Se} and z_{Se}), and bulk modulus (B) and its pressure derivative (B') are reported in Table 1 along with available experimental [19] and theoretical [21, 23] data. From Table 1, one notes that the values of the lattice parameters (a and c) calculated through the LDA are slightly smaller than the corresponding experimental ones, whereas those calculated using the GGA-PBEsol are in excellent agreement with the corresponding measured ones. The relative deviation of the calculated lattice parameter values from the corresponding experimental ones is less than 1.8% when using the LDA functional and about 0.05% when employing the GGA-PBEsol approach. Then, the GGA-PBEsol in addition to the TB-mBJ was adopted in this work to model the exchange–correlation interaction for the remaining studied properties. One notices that previous results [21, 23], calculated using the GGA-PBE, are slightly higher than the measured values [19].

3.2 Elastic Properties

Elastic constants (C_{ij}s) quantify the macroscopic response of crystals to the macroscopic stress and are directly related to many fundamental physical properties, such as mechanical
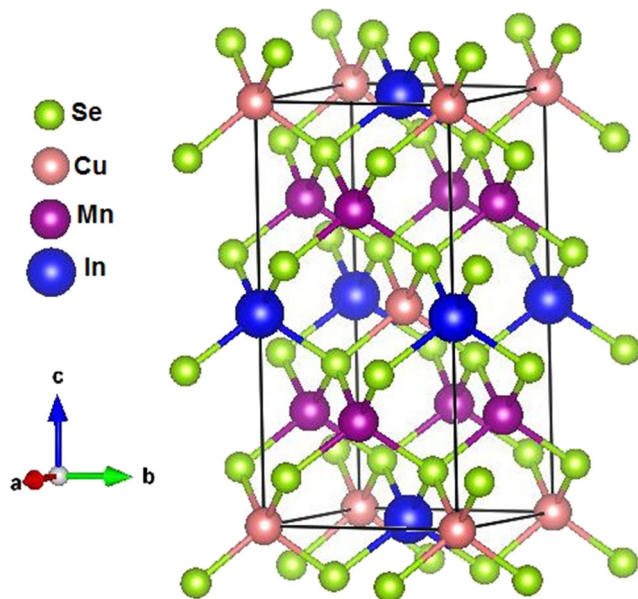

Fig. 1 Conventional unit cell structure of the $CuMn_2InSe_4$ compound

properties, cohesion of solids, and thermodynamic properties [34]. Thus, it is of fundamental and practical interest to calculate the elastic constants of the title compound. The calculated full set elastic constants, namely, C_{11}, C_{33}, C_{44}, C_{66}, C_{12}, and C_{13}, of $CuMn_2InSe_4$ are listed in Table 2. From these data, one can conclude:

(i) The calculated C_{ij}s satisfy the Born-Huang mechanical stability criteria for tetragonal system [35, 36]:

$C_{11} > 0$, $C_{33} > 0$, $C_{44} > 0$, $C_{66} > 0$, $C_{11} - C_{12} > 0$, $C_{11} + C_{33} - 2C13 > 0$, $2C_{11} + C_{33} + 2C_{12} + 4C_{13} > 0$

This implies the mechanical stability of $CuMn_2InSe_4$.

(ii) The moderate values of the elastic constants indicate the moderate resistant of $CuMn_2InSe_4$ to external applied stress.

(iii) $C_{11} = C_{22}$ and C_{33} represent the uniaxial deformation along the [100]/[010] and [001] crystallographic directions, respectively, and the difference between them is a measure of the anisotropy of the elastic properties. The obtained results suggest that the [100]/[010] crystallographic direction is more resistant to uniaxial deformation than the [001] one, indicating the presence of a noticeable structural and elastic anisotropies in the title compound. C_{44} and C_{66} characterize the resistance to the pure shear deformations on the (100)/(010) and (001) crystal planes, respectively. The calculated values for the C_{ij}s demonstrate that the shear deformation in $CuMn_2InSe_4$ is easier than the compressional deformation.

Elastic moduli of the polycrystalline phase of a solid, namely, the bulk modulus (B), shear modulus (G), Young's modulus (E), Poisson's ratio (σ), can be derived from the single crystal elastic constants (C_{ij}s) through the well-known Voigt-Reuss-Hill approximations [37–40]. The calculated values for the aforementioned elastic moduli are listed in Table 2. The obtained results suggest:

(i) The studied compound has a moderate bulk modulus, indicating that its resistant to compression is moderate, i.e., it has a high compressibility. The moderate value of G expresses its moderate resistance to shear deformation. Thus, $CuMn_2InSe_4$ has a moderate hardness.

(ii) The moderate value of the Young's modulus (E) indicates the low resistant to unidirectional compression of $CuMn_2InSe_4$.

(iii) According to the empirical Pugh criterion [41], which assumes that the solid is ductile if $B/G > 1.75$, otherwise brittle, $CuMn_2InSe_4$ is ductile. The main reason of the ductility of $CuMn_2InSe_4$ is attributed to the low value of

Table 1 Calculated equilibrium lattices constants (a and c, in Å), bulk modulus (B, in GPa), first pressure derivative of the bulk modulus (B'), conventional unit cell volume (V, in Å^3), and internal atomic coordinates of the selenium atom (x_{Se} and z_{Se}) for CuMn$_2$InSe$_4$ compared with available experimental and theoretical values

Property	Present work GGA-PBEsol	Present work LDA	Expt.	Others
a	5.8138	5.7049	5.8111[a]	5.86127[b], 5.9436[c]
c	11.515	11.4380	11.5739[a]	11.7684[b], 11.8378[c]
B	60.26	65.15		
B'	4.57	4.417		52.94[c]
V	389.21	372.26	390.84[a]	4.45[c]
c/a	1.981	2.005	1.991[a]	
x_{Se}	0.2343	0.2328		1.991[c]
z_{Se}	0.1252	0.1263		

[a] Ref. [19]

[b] Ref. [21]

[c] Ref. [23]

the shear modulus. A ductile material can resist to thermal shock.

(iv) Debye temperature (T_D), one of the most important physical parameters that characterizes the thermal properties of materials, can be calculated from the average sound velocity (V_m), which can be calculated in turn from the B and G moduli by using the well-known relations [42]. As a rule, the height value of T_D implies a high stiffness, high thermal conductivity, and high associated melting temperature. The relatively low T_D value (Table 2) confirms the moderate stiffness of CuMn$_2$InSe$_4$ and reveals its low thermal conductivity, which is a required criterion for a performant thermoelectric material.

Evaluation of the extent of elastic anisotropy of crystals is extremely important in engineering and crystal physics because its correlation with the possibility of inducing microcracks in materials [43] and its significant influence on the nanoscale precursor textures in alloys [44]. Elastic anisotropy is related to the difference in bonding character in different crystallographic directions. Some indexes have been developed to evaluate the extent of the elastic anisotropy in materials. Two different criteria were used to determine the degree of the elastic anisotropy of CuMn$_2$InSe$_4$, namely, the universal factor (A^U) and 3D representation of the crystallographic direction dependence of the Young's modulus and Bulk modulus.

(i) The universal factor (A^U) is defined as [45] $A^U = 5G_V/G_R + B_V/B_R - 6$, where the subscripts V and R stand to Voigt and Reuss approximations [37, 38]. For an elastically isotropic crystal, $A^U = 0$. Therefore, the degree of deviation of A^U from zero characterizes the extent of the elastic anisotropy of the crystal. Calculated value of A^U (0.41) indicates that CuMn$_2$InSe$_4$ exhibits a pronounced elastic anisotropy.

(ii) 3D representation of the crystallographic direction dependence of elastic moduli, such as the Young's modulus and bulk modulus, is a widely used tool to visualize the extent of the elastic anisotropy of crystals. For an elastically isotropic crystal, the 3D representation (a closed surface) shows a perfect spherical shape. Thus, the degree of deviation of this closed surface from the spherical shape measures the extent of the anisotropy of the considered modulus. Crystallographic direction dependence of the Young's modulus (E) and compressibility ($\beta = 1/B$) of a tetragonal system in a spherical system is given by the following relationships [46]:

$$\beta = B^{-1} = (S_{11} + S_{12} + S_{13})(l_1^2 + l_2^2) + (2S_{13} + S_{33})l_3^2$$

$$E^{-1} = S_{11}(l_1^4 + l_2^4) + (2S_{13} + S_{44})(l_1^2 l_3^2 + l_2^2 l_3^2) + S_{33}l_3^4 + (2S_{12} + S_{66})l_1^2 l_2^2$$

Here, l_1, l_2, and l_3 are the direction cosines in spherical coordinates with respect to x-, y-, and z-axes and S_{ij} are the elastic compliances. The calculated 3D representations of the directional dependence of the Young's modulus (E) and compressibility (β) and their cross sections in the xy and xz planes are shown in Fig. 2. Obviously, the 3D-closed surfaces (cross sections) of E and β exhibit a pronounced deviation from the spherical shape (circular form), indicating a noticeable directional dependence of the Young modulus and compressibility.

Table 2 Calculated single elastic constants (C_{ij}, in GPa), bulk modulus (B, in GPa), shear modulus (G, in GPa), Young's modulus (E, in GPa), Poisson's ratio (σ, dimensionless), average sound velocity (V_m, in m/s), Debye temperature (T_D, in K), and anisotropy factor (A^U, dimensionless) for CuMn$_2$InSe$_4$

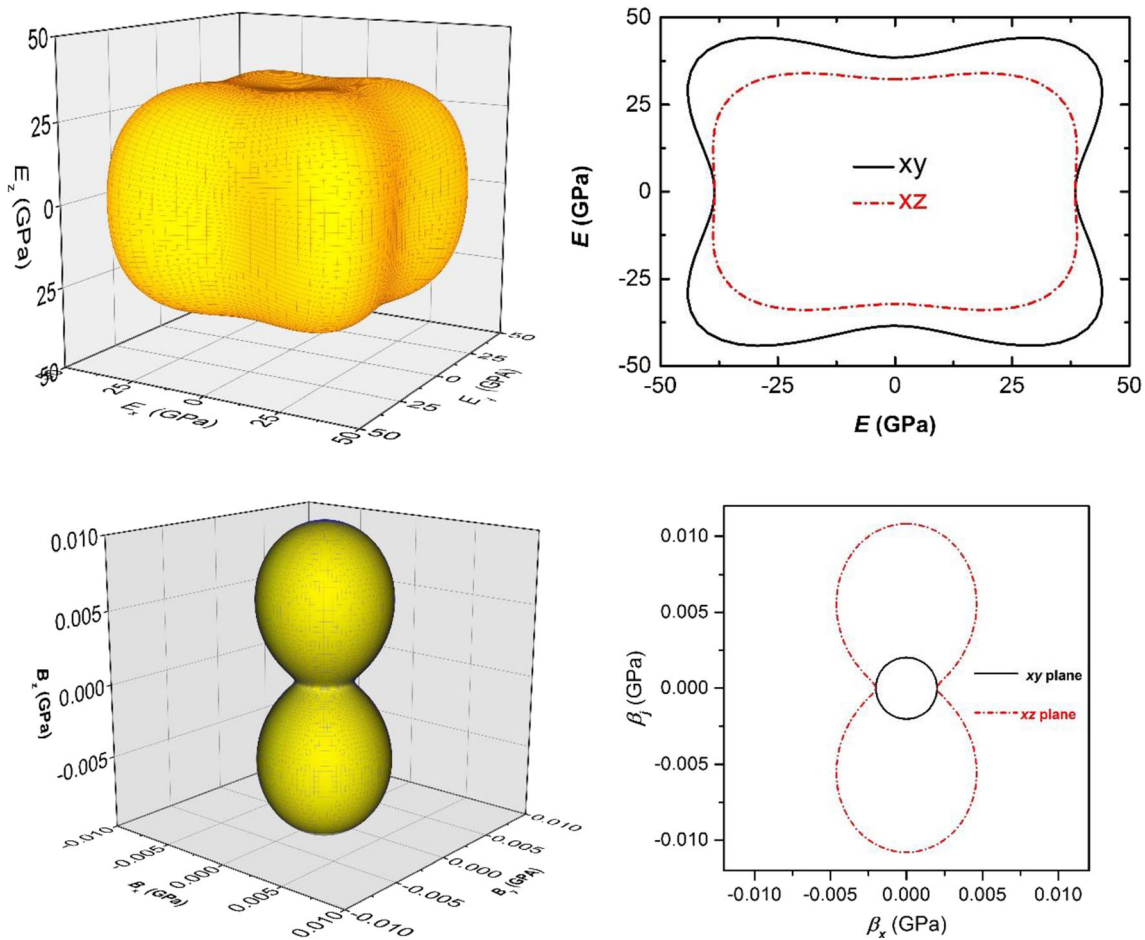|	C_{11}	C_{33}	C_{44}	C_{66}	C_{12}	C_{13}
	102.8	70.5	18.3	21.7	72.7	58.8
B	G	E	σ	V_m	T_D	A^U
70.72	16.6		0.3895	1885.9	202.5	0.4129

Fig. 2 The directional dependence of the Young's modulus and compressibility as well as their cross sections in the *xy* (001) and *xz* planes (010) crystallographic planes

Thus, one concludes that $CuMn_2InSe_4$ is characterized by a pronounced elastic anisotropy.

3.3 Electronic and Magnetic Properties

Figure 3 shows the calculated band structures for spin-up and spin-down channels along the high symmetry lines in the Brillouin zone (BZ) of $CuMn_2InSe_4$ at its optimized structural parameters using the TB-mBJ potential. As it can be seen from Fig. 3, the DLQS $CuMn_2InSe_4$ evidences a semiconducting nature for both spin polarization channels. For the spin-up channel, both the top of the valence band (VBM) and the bottom of the conduction band (CBM) occur at the center of BZ, demonstrating that this compound is a direct energy band gap ($\Gamma^V - \Gamma^C$) semiconductor for the spin-up channel; the band gap value is equal to 0.904 eV. For the spin-down channel, both the VBM, which is below the Fermi level, and the CBM are located at the Z-point in BZ, revealing that this compound is a direct energy band gap ($Z^V - Z^C$) semiconductor for the spin-down channel; the band gap value is equal to 1.403 eV. Therefore, the spin-polarized $CuMn_2InSe_4$ crystal has an indirect band gap ($\Gamma^V - Z^C$) of about 0.667 eV. Thus,

our present result reveals that $CuMn_2InSe_4$ is a semiconductor and this contrasts with what were previously predicted by [21, 23]. By using the FP-LAPW method with the GGA-PBE functional, Berri [21] reported that $CuMn_2InSe_4$ exhibits a half-metallic character with a zero gap for the spin-up channel and a direct band gap of 1.10 eV for the spin-down one. By using the PP-PW approach with the GGA-PBE functional, Yan et al. [23] predicted a zero gap for the spin-up channel and an indirect band gap ($\Gamma - Z$) of 1.01 eV for the spin-down channel. One notes the disagreement between the results of these two aforementioned references concerning the value and nature of the spin-down channel band gap. Unfortunately, experimental data relating to the band gap of $CuMn_2InSe_4$ are not available in the literature at this moment to make a meaningful comparison in order to testify all these different theoretical predictions. One notices that the CBM is more dispersive than the VBM, insinuating that the hole effective mass of $CuMn_2InSe_4$ would be greater than the electron one, but in return the hole mobility would be smaller than the electron one.

For deep information about the distribution of electronic states in the energy spectrum, the total and atom and

Fig. 3 Calculated band structure for spin-up and spin-down channels of $CuMn_2InSe_4$ using the TB-mBJ potential
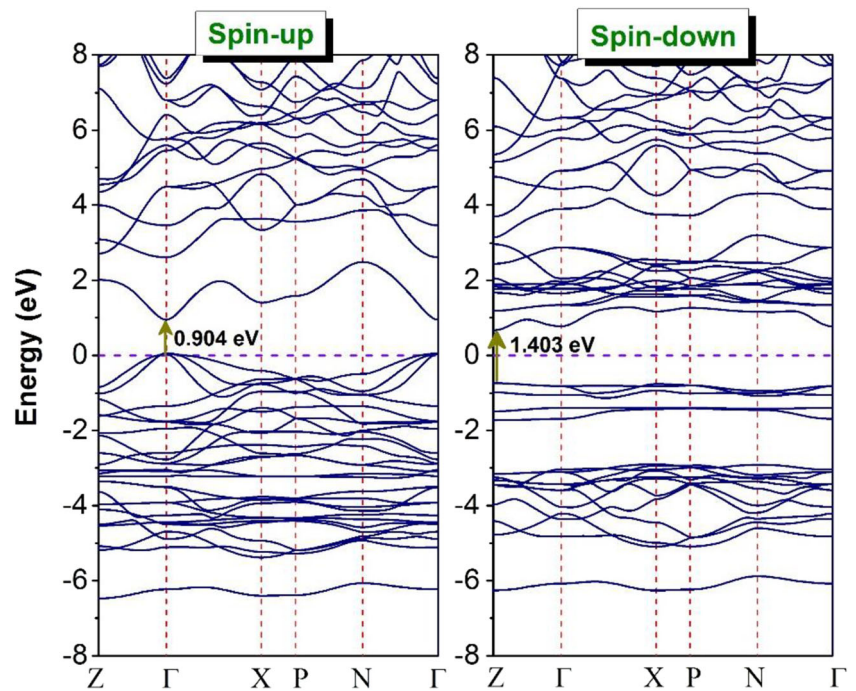
angular-momentum resolved density of states (TDOS and PDOS) curves were calculated and depicted in Fig. 4 for both spin-up and spin-down channels of $CuMn_2InSe_4$. As an initial analysis, one notes the asymmetry of the TDOS and PDOS curves. The DOS of the majority spin channel can be divided into five energy regions, including four valence band groups and a conduction band group separated by band gaps. Region

I, from -16.12 to -15.78 eV, consists of the In-d states. Region II, from -14.00 to -12.85 eV, originates mainly from the Se-s states with a small contribution from the In-d states. Region III, from -6.5 to -5.85 eV, is formed from In-s and Se-p states. Region IV, from -5.5 eV to Fermi level E_F, shows 12 sharp sub-bands. The lower part of the region IV is dominated by the hybridized Se-p and Mn-d states, and the higher

Fig. 4 Calculated total and atom and angular-momentum resolved densities of states (TDOS and PDOS) for the $CuMn_2InSe_4$ compound
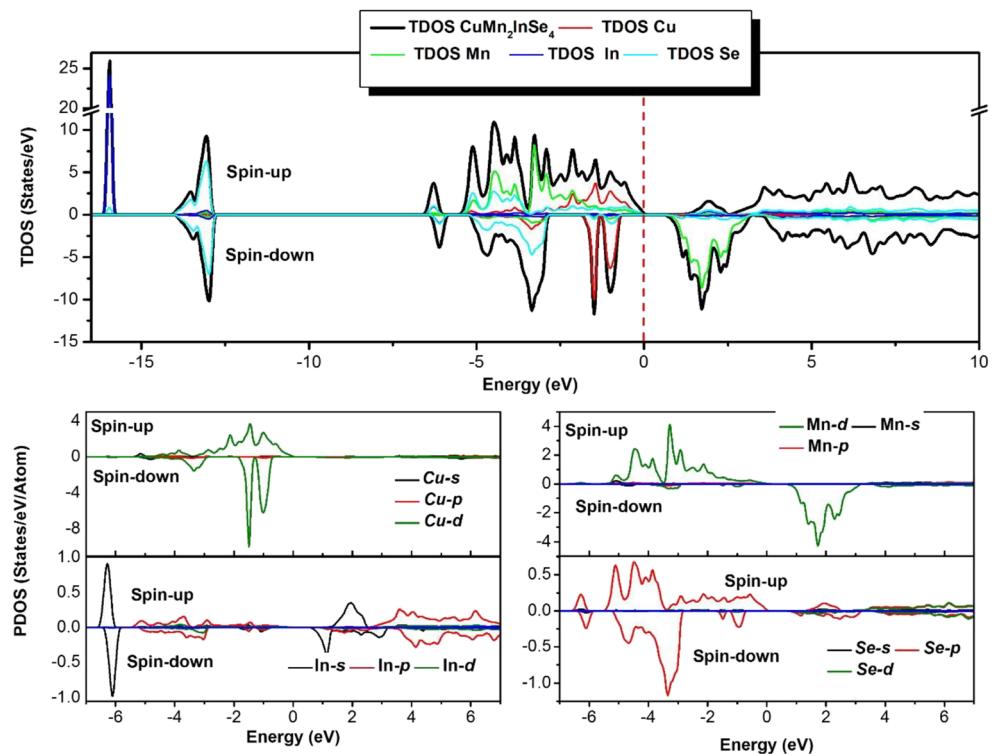
one is composed of the hybridized Cu-*d*, Mn-*d*, and Se-*p* states. These hybridizations reflect the dominant covalent bonding between these atoms. Finally, the lower part of the region V—conduction band group—is due to the hybridized In-*s* and Se-*p* states, while the higher part is dominated by the In-*p* and Se-*d* states. The lowest valence band group in the DOS diagram of the spin-up channel is absent in the DOS diagram of the spin-down channel. The highest valence band group splits into two separated groups: the lower one, from −6.34 to −5.87 eV, is dominated by the Se-*p* states with a small contribution from the Cu-*d* and the higher one, from −5.19 to −2.84 eV, is formed mainly by the Cu-*d* states. The lower part of the conduction band is essentially composed of the Mn-*d* orbitals. The asymmetry of the DOS curves of $CuMn_2InSe_4$ is due to the asymmetries of the DOS of the Mn and Cu atoms. From the DOS diagrams, one notes that the main peaks of the Cu-3*d* and Mn-3*d* PDOS emerge at different energies, indicating the weaker hybridization between the Cu-3*d* and Mn-3*d* states in $CuMn_2InSe_4$ compound. In addition, it is seen that the electronic properties of $CuMn_2InSe_4$ depend mostly on the Mn and Cu atoms.

For a deep analysis of the interatomic bonding, the valence electron charge density distribution maps in the (1 0 0) and (012) crystallographic planes are depicted in Fig. 5. These maps indicate the predominant covalent bonding nature of the In-Se, Cu-Se, and Mn-Se bonds due the hybridization of the (In-*s*, Se-*p*), (Cu-*d*, Se-*p*), and (Mn-*d*, Se-*p*) states.

Calculated total and local magnetic moments for $CuMn_2InSe_4$ using the TB-mBJ potential are summarized in Table 3 along with previous calculations. The most of the magnetic moment arises from the Mn-3*d* states with small contributions from the interstitial region and the other constituent atoms. The calculated total magnetic moment for $CuMn_2InSe_4$ is in agreement with previous theoretical results [21, 23].

Table 3 Calculated total, interstitial, and atomic magnetic moments (in μ_B) along with previous results for $CuMn_2InSe_4$

	M_{tot}	$M_{Interstitial}$	M_{Cu}	M_{Mn}	M_{Se}	M_{In}
Present	10	0.75	0.09	4.43	0.06	0.05
Others	10[a]	0.86[a]	0.11[a]	4.34[a]	0.06[a]	0.05[a]
	10[b]	-	0.13[b]	4.43[b]	0.21[b]	0.14[b]

[a] Ref. [21]

[b] Ref. [23]

3.4 Optical Properties

Linear response of a material to an incident electromagnetic radiation is represented by the dielectric function $\varepsilon(\omega)$. The dielectric function $\varepsilon(\omega)$ is a complex function: $\varepsilon(\omega) = \varepsilon_1(\omega) + i\varepsilon_2(\omega)$, where the real part $\varepsilon_1(\omega)$ characterizes the dispersion of the incident radiation by the medium and the imaginary one $\varepsilon_2(\omega)$ describes the absorbed energy by the medium. Theoretically, the $\varepsilon_2(\omega)$ spectrum can be calculated from the band structure through well-known relationship [47]. The real part $\varepsilon_1(\omega)$ can be calculated from $\varepsilon_2(\omega)$ through the Kramer–Kronig transformation. All remaining linear optical functions, such as the absorption coefficient $\alpha(\omega)$, refraction index $n(\omega)$, extinction coefficient $k(\omega)$, reflectivity $R(\omega)$, and electron energy-loss function $L(\omega)$, can be calculated from $\varepsilon_1(\omega)$ and $\varepsilon_2(\omega)$ via well-known relationships. The calculated $\varepsilon_1(\omega)$ and $\varepsilon_2(\omega)$ spectra for the studied system are illustrated in Fig. 6. As a result of the tetragonal symmetry of the studied material, only the dielectric components ε^{xx} and ε^{zz} are considered. The dielectric components ε^{xx} and ε^{zz} correspond to the responses of the medium to the incident radiation polarized along the *x*- and *z*-axes, respectively. We note a considerable optical anisotropy in $\varepsilon_1(\omega)$ and $\varepsilon_2(\omega)$ spectra in the
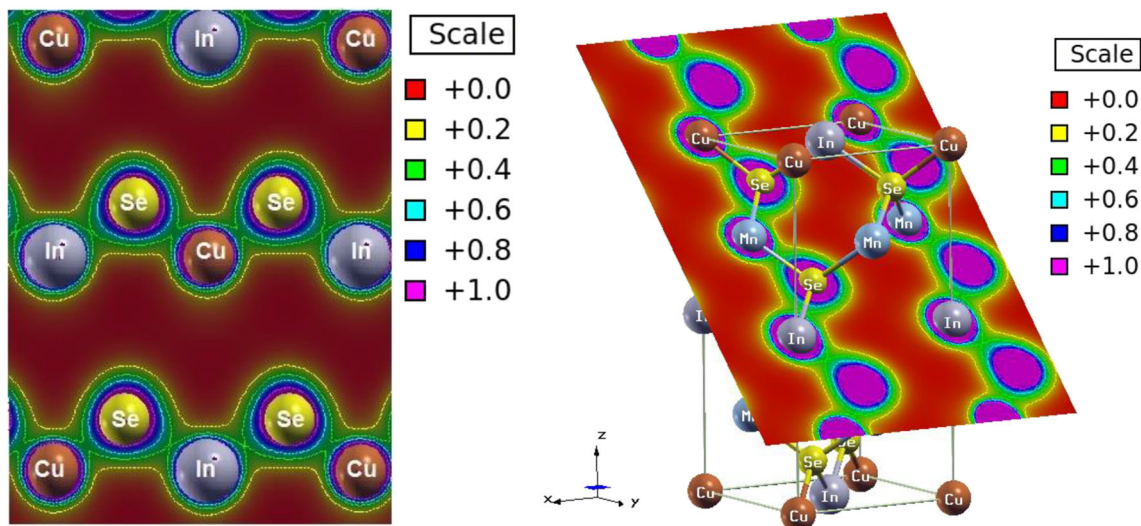

Fig. 5 Calculated electronic charge distribution maps in the (100) (left panel) and (012) (right panel) crystallographic planes for the $CuMn_2InSe_4$ compound
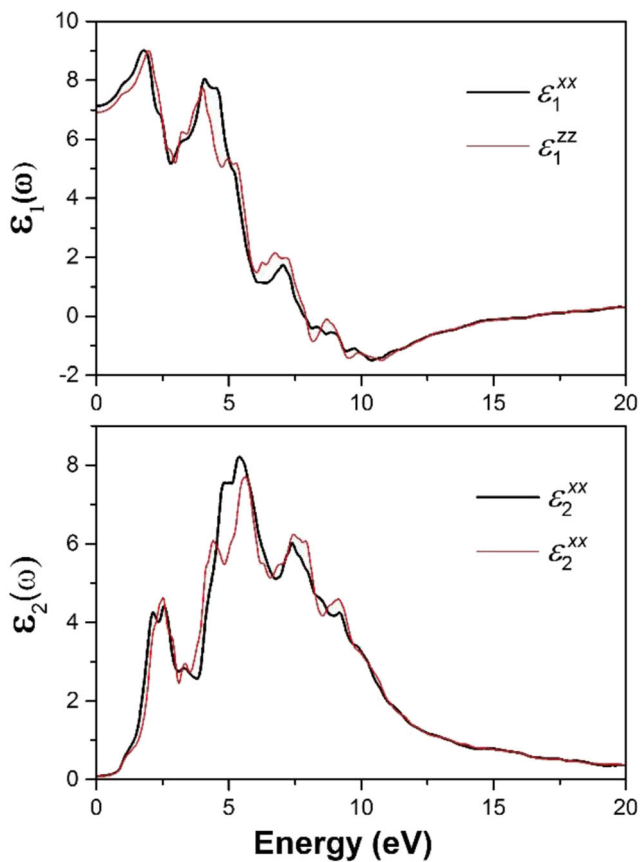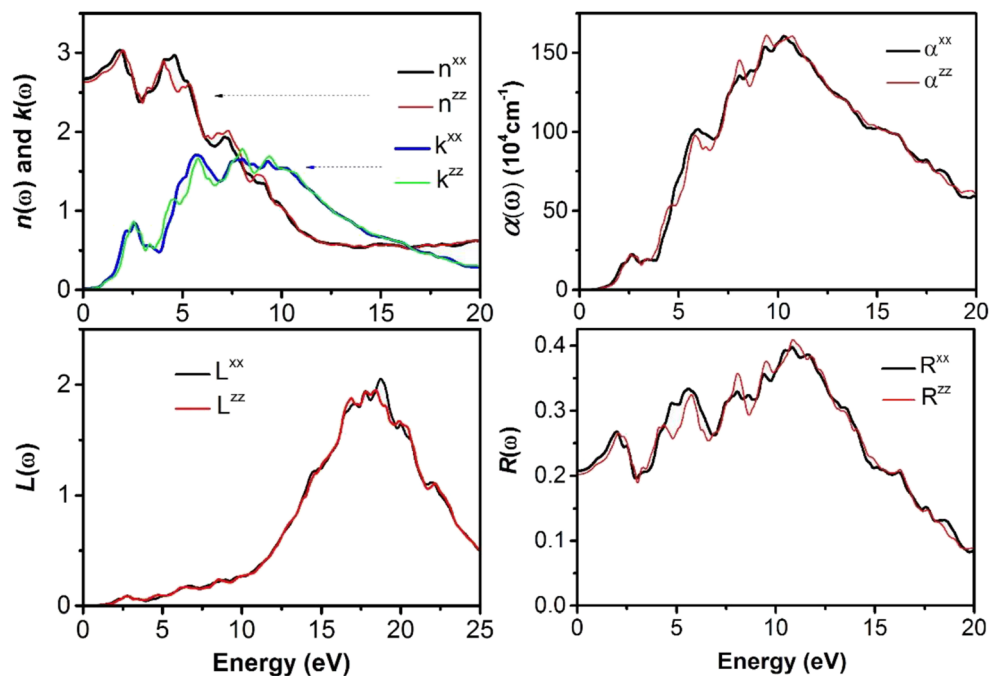
Fig. 6 Calculated real ($\varepsilon_1(\omega)$) and imaginary ($\varepsilon_2(\omega)$) parts of the dielectric function for CuMn$_2$InSe$_4$

of the electronic structure. The main peaks of the $\varepsilon_2(\omega)$ spectra are due principally to the electronic transitions from the Cu-d and Mn-d occupied valence states to the Mn-d and Se-p empty conduction ones. The first critical point of $\varepsilon_2(\omega)$, known as the fundamental absorption edge, is originated from the direct electronic transition from the valence band maxima to the conduction band minima at the Γ-point. The $\varepsilon_2^{xx}(\omega)$ and $\varepsilon_2^{zz}(\omega)$ spectra start at the same energy, indicating an isotropic energy gap. ε_1^{xx} (ε_1^{zz}) rises with increasing photon energy to attain its maximum at 1.80 (1.99) eV and then decreases subsequently. The static dielectric constants $\varepsilon_1^{xx}(0) = \varepsilon_1^{xx}(\omega \to 0)$ and $\varepsilon_1^{zz}(0) = \varepsilon_1^{zz}(\omega \to 0)$ for the title compound are equal to 7.18 and 6.92, respectively.

The absorption coefficient $\alpha(\omega)$, refraction index $n(\omega)$, extinction coefficient $k(\omega)$, reflectivity $R(\omega)$, and electron energy-loss function $L(\omega)$ for incident radiation polarized along the a and c axes for a spectral region up to 20 eV are plotted in Fig. 7. These spectra exhibit a noticeable optical anisotropy. The refractive index n^{xx} (n^{zz}) reaches its maximum at about 1.9 (2.01) eV. Calculated static refractive index $n^{xx}(0)$ ($n^{zz}(0)$) is equal to 3.15 (3.15). The optical absorption coefficient $\alpha(\omega)$ shows that the title compound is characterized by a high optical absorption ($> 10^4$ cm^{-1}) in a broad energy range in the ultra violet range between 5 and 20 eV. A maximum reflectivity R^{xx} (R^{zz}) of about 40% occurs at 10.83 (10.93) eV.

3.5 Thermoelectric Properties

Thermoelectric (TE) materials are able to convert directly heat into electricity by using Seebeck effect or pump heat for

energy range from 2.06 to 9.83 eV, whereas they are mostly isotropic in the higher energy region. This optical anisotropy is expected due to the crystal low symmetry and the influence

Fig. 7 Calculated refractive index $n(\omega)$, extinction coefficient $k(\omega)$, absorption coefficient $\alpha(\omega)$, optical reflectivity $R(\omega)$, and energy-loss function $L(\omega)$ for CuMn$_2$InSe$_4$

cooling by using Peltier effect [48]. Efficiency of the energy conversion devices for harvesting waste heat and converting it into usable electrical energy is overseen by a dimensionless parameter that is called figure of merit (ZT), defined as: $ZT = S^2\sigma T/(\kappa_e + \kappa_L)$, where S is the Seebeck coefficient (thermopower), σ is the electrical conductivity, T is the absolute temperature, and κ_e and κ_L are the electronic and lattice thermal conductivities of the material, respectively. A large value of ZT means higher thermoelectric conversion efficiency. Thus, to obtain a performant thermoelectric device, the TE material used in making this device should have a high Seebeck coefficient and high electrical conductivity (often referred to as having high power factor: $PF = S^2\sigma$) and low thermal conductivity simultaneously. In other words, efficient TE material entails low thermal conductivity and good electronic transport properties simultaneously. As the title material crystallizes in a tetragonal structure, we calculated the average and diagonal components of the thermoelectric coefficients. Figure 8 shows the xx (along the a-axis; $\vec{x}//\vec{a}$) and zz (along the c-axis; $\vec{z}//\vec{c}$) components, and the average (the arithmetic average between the xx, yy, and zz components) of the basic transport parameters, namely, the Seebeck

coefficient (S), electrical conductivity scaled by relaxation time (σ/τ), electronic thermal conductivity scaled by relaxation time (κ_e/τ), and power factor scaled by relaxation time ($PF = S^2\sigma/\tau$) as function of μ-E_F, where μ is the chemical potential and E_F is the Fermi level energy, from -0.5 to 1.5 eV at three different fixed temperatures, namely, $T = 300$ K, 600 K, and 900 K. It is worth to note that within the rigid-band shift model, the chemical potential determines the carrier concentration of the compound. In the case of n-type doping, the Fermi level gets upshifted, which corresponds to positive μ-E_F and for p-type doping, the Fermi level shifts down and the corresponding μ-E_F is negative [49]. From Fig. 8, one notes that the curves of the S^{xx} and S^{zz} components as function of chemical potential are almost superposed, indicating that the Seebeck coefficient of CuMn$_2$InSe$_4$ is almost isotropic, i.e., independent of the crystallographic directions. The Seebeck coefficient of intrinsic (undoped) CuMn$_2$InSe$_4$, i.e., S value at $\mu - E_F = 0$, is positive, suggesting that the hole-type charge carriers would dominate the thermoelectric transport in this compound. The average Seebeck coefficient $S = 1/3(S^{xx} + S^{yy} + S^{zz})$ value at $\mu - E_F = 0$ is about 251 μVK^{-1} at $T = 300$ K, 245 μVK^{-1} at $T = 600$ K, and 237 μVK^{-1} at $T = 900$
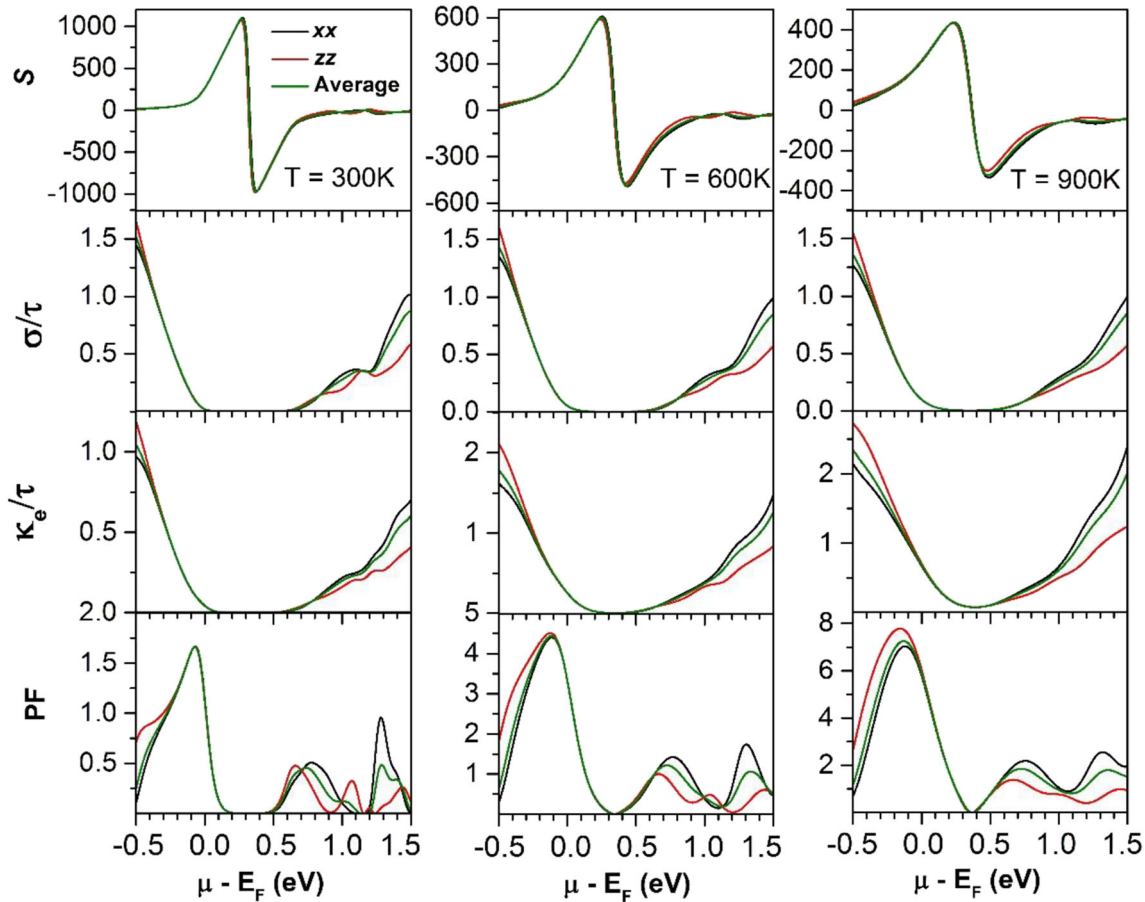

Fig. 8 Chemical potential (μ-E_F) dependence of the average and components along the a and c axes of the Seebeck coefficient (S, in μVK^{-1}), electrical conductivity over relaxation time (σ/τ, in $10^{20}\Omega^{-1}$m^{-1}s^{-1}), electronic thermal conductivity (κ_e, in 10^{15}Wm^{-1}K^{-1}s^{-1}), and power factor (PF, in 10^{11}WK^{-1}m^{-1}s^{-1}) at three different temperatures: 300, 600, and 600 K for CuMn$_2$InSe$_4$

K. These results corroborate that $CuMn_2InSe_4$ might be as efficient as the well-known thermoelectric materials but its maximum ZT value could not be larger than 1. The thermopower decreases with increasing charge carrier concentration, which is consistent with the common semiconductor behavior. For the same charge carrier concentration, the S value for the hole doping (positive S value area) is somewhat larger than that for the electron doping (negative S value area), suggesting that the p-type would perhaps be more favorable for TE properties than the n-doped one. The electrical conductivity exhibits a noticeable anisotropy, especially for the n-doped case. The value of electrical conductivity for negative chemical potential is higher than that of the positive one, indicating the p-doped compound will have higher electrical conductivity than the n-doped one. Figure 8 clearly shows the strong doping dependence of the electrical conductivity of the studied compound. The electrical conductivity increases strongly with increasing charge carrier concentration. It is evident from Fig. 8 that the thermal conductivity is noticeably anisotropic. The power factor shows certain directional dependence behavior, especially in the n-doped region. The PF value along the a-axis is somewhat larger than that along the c-axis. To increase the figure of merit ($ZT = S\sigma^2/\kappa$), the power factor ($PF = S^2\sigma$) should be as large as possible. The thermoelectric performance of the title compound can be optimized by appropriate doping concentration (the optimum doping concentration), which corresponds to the maximum value of the power factor around the Fermi level. The average power factor ($APF = (2PF^{xx} + PF^{\varepsilon z})/3$) exhibits two peaks in the vicinity of the Fermi level. Maximum values of the APF in the p- and n-doped regions and the corresponding chemical potential (μ-E_F), charge carrier concentration (n), Seebeck coefficient (S), electrical conductivity, and thermal conductivity at three different temperatures (300, 600, and 900 K) are listed in Table 4. Figure 8 shows that the value of the power factor over relaxation time $S^2\sigma/\tau$ at the optimal carrier concentration for the p-type $CuMn_2InSe_4$ is larger than that for the n-type one. One notes that the PF peak around the Fermi level in the p-doped region (negative μ-E_F) shifts to higher p-doping levels (larger number of chemical potential) with increasing temperature from 300 to 900 K, and there is a significant

increase in its value. In the n-doped region (positive μ-E_F), the PF peak does not move but there is a significant increase in its value with increasing temperature from 300 to 900 K.

4 Conclusions

In summary, the structural, elastic, electronic, optical, and thermoelectric properties of the recently synthesized quaternary diamond-like semiconductor $CuMn_2InSe_4$ were investigated via first-principles calculations based on density functional theory combined with the Boltzmann transport theory. Present interesting findings are:

(i)   Calculated structural parameters are in excellent agreement with available experimental data.
(ii) Calculated single-crystal and polycrystalline elastic moduli suggest that $CuMn_2InSe_4$ is a soft material, mechanically stable, and elastically anisotropic.
(iii) Calculated band structure reveals that the title compound has a direct energy gap ($\Gamma^V - \Gamma^C$) of about 0.904 eV for the spin-up channel that turns out to be a $Z^V - Z^C$ direct gap of about 1.403 eV for the spin-down channel, which result in an indirect gap ($\Gamma^V - Z^C$) of about 0.667 eV for the spin-polarized $CuMn_2InSe_4$.
(iv) Calculated density of states diagram and charge density distribution map show that the studied compound exhibits a strong covalent In-Se, Cu-Se, and Mn-Se bonding due the hybridization of the (In-s, Se-p), (Cu-d, Se-p), and (Mn-d, Se-p) states.
(v)   Linear optical functions were predicted for a large energy range up to 20 eV.
(vi) Calculated total magnetic moment is principally originated from the Mn-d electronic states.
(vii) Chemical potential dependence of the thermoelectric parameters was predicted. It is found that the studied compound has high power factor for p-type doping.

The obtained results could provide guidance for future experimental work.

Table 4   Calculated maximum values of the average power factor (PF, in $10^{11} Wm^{-1}K^{-1}s^{-1}$) in the p- and n-doped regions and the corresponding chemical potential (μ-E_F, in eV) and Seebeck coefficient (S, μVK^{-1}) for the $CuMn_2InSe_4$ compound

	300		600		900	
	p-type	n-type	p-type	n-type	p-type	n-type
μ-E_F	− 0.07	0.73	− 0.12	0.72	− 0.13	0.72
PF	1.66	0.46	4.42	1.21	7.27	1.87
S	111	− 99	139	− 156	146	− 170

References

1. Sevik, C., Çağın, T.: Ab initio study of thermoelectric transport properties of pure and doped quaternary compounds. Phys. Rev. B. **82**, 045202–045207 (2010)
2. Liu, M.L., Chen, I.W., Huang, F.Q., Chen, L.D.: Improved thermoelectric properties of Cu-Doped quaternary chalcogenides of $Cu_2CdSnSe_4$. Adv. Mater. **21**, 3808–3812 (2009)

3. Sevik, C., Cagin, T.: Ab initio study of thermoelectric transport properties of pure and doped quaternary compounds. Phys. Rev. B. **82**, 045202–045206 (2010)

4. Shi, X.Y., Huang, F.Q., Liu, M.L., Chen, L.D.: Thermoelectric properties of tetrahedrally bonded wide-gap stannite compounds $Cu_2ZnSn_{1-x}In_xSe_4$. Appl. Phys. Lett. **94**, 122103–122105 (2009)

5. Song, Q., Qiu, P., Hao, F., Zhao, K., Zhang, T., Ren, D., Shi, X., Chen, L.: Quaternary pseudocubic $Cu_2TMSnSe_4$ (TM = Mn, Fe, Co) chalcopyrite thermoelectric materials. Adv. Electron. Mater. 1600312–1600318 (2016)

6. Ford, G.M., Guo, Q., Agrawal, R., Hillhouse, H.W., Hugh, W.: Earth abundant element $Cu_2Zn(Sn_{1-x}Ge_x)S_4$ nanocrystals for tunable band gap solar cells: 6.8% efficient device fabrication. Chem. Mater. **23**, 2626–2629 (2011)

7. Brunetta, C.D., Minsterman, W.C., Lake, C.H., Aitken, J.A.: Cation ordering and physic chemical characterization of the quaternary diamond-like semiconductor Ag_2CdGeS_4. J. Solid State Chem. **187**, 177e185 (2012)

8. Khyzhun, O.Y., Bekenev, V.L., Ocheretova, V.A., Fedorchuk, A.O., Parasyuk, O.V.: Electronic structure of $Cu_2ZnGeSe_4$ single crystal: ab initio FP-LAPW calculations and X-ray spectroscopy measurements. Phys. B. **461**, 75e84 (2015)

9. Liu, B.W., Zhang, M.J., Zhao, Z.Y., Zeng, H.Y., Zheng, F.K., Guo, G.C., Huang, J.S.: Synthesis, structure, and optical properties of the quaternary diamond-like compounds I2-II-IV-VI4 (I = Cu; II = Mg; IV = Si, Ge; VI = S, Se). J. Solid State Chem. **204**, 251e256 (2013)

10. Bedjaoui, A., Bouhemadou, A., Aloumi, S., Khenata, R., Bin-Omran, S., Al-Douri, Y., Saad Saoud, F., Bensalem, S.: Structural, elastic, electronic and optical properties of the novel quaternary diamond-like semiconductors Cu_2MgSiS_4 and Cu_2MgGeS_4. Solid State Sciences. **70**, 21–35 (2017)

11. Chambers, S.A., Yoo, Y.K.: New materials for spintronics. MRS Bull. **28**, 706–710 (2003)

12. Steinhagen, C., Panthani, M.G., Akhavan, V., Goodfellow, B., Koo, B., Korgel, B.A.: Synthesis of Cu_2ZnSnS_4 nanocrystals for use in low-cost photovoltaics. J. Am. Chem. Soc. **131**, 12554–12555 (2009)

13. Guo, Q., Ford, G.M., Yang, W.C., Walker, B.C., Stach, E.A., Hillhouse, H.W., Agrawal, R.: Fabrication of 7.2% efficient CZTSSe solar cells using CZTS nanocrystals. J. Am. Chem. Soc. **132**, 17384–17386 (2010)

14. Chen, S., Gong, X.G., Walsh, A., Wei, S.H.: Electronic structure and stability of quaternary chalcogenide semiconductors derived from cation cross substitution of II-VI and I-III-VI$_2$ compounds. Phys. Rev. B. **79**, 165211–165218 (2009)

15. Schnabel, T., Low, M., Ahlswede, E.: Vacuum-free preparation of 7.5% efficient $Cu_2ZnSn(S/Se)_4$ solar cells based on metal salt precursors. Sol. Energy Mater. Sol. Cells. **117**, 324–328 (2013)

16. Fella, C.M., Romanyuk, Y.E., Tiwari, A.N.: Technological status of $Cu_2ZnSn(S,Se)_4$ thin film solar cells. Sol. Energy Mater. Sol. Cells. **119**, 276–277 (2013)

17. Levcenco, S., Dumcenco, D., Huang, Y.S., Arushanov, E., Tezlevan, V.: Polarization dependent electrolyte electro reflectance study of Cu_2ZnSiS_4 and $Cu_2ZnSiSe_4$ single crystals. J. Alloys Comp. **509**, 7105–7108 (2011)

18. Li, Y., Fan, W., Sun, H., Cheng, X., Li, P., Zhao, X.: Electronic, optical and lattice dynamic properties of the novel diamond-like semiconductors Li_2CdSiS_4 and Li_2CdSnS_4. J. Phys. Condens. Matter. **23**, 225401–225411 (2011)

19. Lekse, J.W., Moreau, M.A., McNerny, K.L., Yeon, J., Halasyamani, P.S.: Second harmonic generation and crystal structure of the diamond-like semiconductors Li_2CdSiS_4 and Li_2CdSnS_4. J.A. Aitken. Inorg. Chem. **48**, 7516–7518 (2009)

20. Delgado, G.E., Sagredo, V.: Crystal structure of the new diamond-like semiconductor $CuMn_2InSe_4$. Bull. Mater. Sci. **39**, 1631–1634 (2016)

21. Delgado, G.E., Grima-Gallardo, P., Nieves, L., Cabrera, H., Glenn, J.R., Aitken, J.A.: Structural characterization of two new quaternary chalcogenides: $CuCo_2InTe_4$ and $CuNi_2InTe_4$. Materials Research. **19**, 1423–1428 (2016)

22. Berri, S.: Search for new half-metallic ferromagnets in quaternary diamond-like compounds I–II2–III–VI4 and I2–II–IV–VI4 (I = Cu; II = Mn, Fe, Co; III = In; IV = Ge, Sn; VI = S, Se, Te). J. Superconductivity Novel Magnet. **31**, 1941–1947 (2017)

23. Perdew, J.P., Burke, K., Ernzerhof, M.: Generalized gradient approximation made simple. Phys. Rev. Lett. **77**, 3865(1-4) (1996)

24. Han, Y., Khenata, R., Li, T., Wang, L., Wang, X.: Search for a new member of parabolic-like spin-gapless semiconductors: the case of diamond-like quaternary compound $CuMn_2InSe_4$. Results in Physics. **10**, 301–303 (2018)

25. Becke, A.D., Johnson, E.R.: A simple effective potential for exchange. J. Chem. Phys. **124**, 221101 (1-4) (2006)

26. Tran, F., Blaha, P.: Accurate band gaps of semiconductors and insulators with a semi-local exchange-correlation potential. Phys. Rev. Lett. **102**, 226401 (1-4) (2009)

27. Jiang, H.: Band gaps from the Tran-Blaha modified Becke-Johnson approach: a systematic investigation. J. Chem. Phys. **138**, 134115–134117 (2013)

28. Koller, D., Tran, F., Blaha, P.: Merits and limits of the modified Becke-Johnson exchange potential. Phys. Rev. B. **83**, 195134–195110 (2011)

29. Singh, D.J.: Structure and optical properties of high light output halide scintillators. Phys. Rev. B. **82**, 155145–155110 (2010)

30. Singh, D.J.: Electronic structure calculations with the Tran-Blaha modified Becke-Johnson density functional. Phys. Rev. B. **82**, 205102–205110 (2010)

31. P. Blaha, K. Schwarz, G.K. H. Madsen, D. Kvasnicka, J. Luitz, R. Laskowski, F. Tran, L. D. Marks: WIEN2k, an augmented plane wave + local orbitals program for calculating crystal properties (Karlheinz Schwarz, Techn. Universität Wien, Austria), 2018. ISBN 3-9501031-1-2

32. Perdew, J.P., Wang, Y.: Accurate and simple analytic representation of the electron-gas correlation energy Phys. Rev. B. **45**, 13244–13249 (1992)

33. Perdew, J.P., Ruzsinszky, A., Csonka, G.I., Vydrov, O.V., Scuseria, G.E., Constantin, L., Burke, K.: Restoring the density-gradient expansion for exchange in solids and surfaces. Phys. Rev. Lett. **100**, 136406 (1-4) (2008)

34. Madsen, G.K.H., Singh, D.J.: BoltzTraP. A code for calculating band-structure dependent quantities. Comput. Phys. Commun. **175**, 67–71 (2006)

35. Yu, R., Zhu, J., Ye, H.Q.: Calculations of single-crystal elastic constants made simple. Computer Physics Communications. **181**, 671–675 (2010)

36. Born, M., Huang, K.: Dynamics theory of crystal lattices. Oxford University Press, Oxford (1954)

37. He, T.W., Jiang, Y.H., Zhou, R., Feng, J.: The electronic structure, mechanical and thermodynamic properties of Mo_2XB_2 and MoX_2B_4 (X_5Fe, Co, Ni) ternary borides. J. App. Phys. **118**, 075902–075913 (2015)

38. Voigt, W.: Lehrbuch der Kristallphysik (Textbook of Crystal Physics). Taubner, Leipzig (1928)

39. Reuss, A.: Berechnung der Fließgrenze von Mischkristallen auf Grund der Plastizitätsbedingung für Einkristalle (calculation of the yield strength of solid solutions based on the plasticity condition of single crystals). Angew Z Math Mech. **9**, 49–58 (1929)

40. Hill, R.: The elastic behavior of a crystalline aggregate. Proc. Phys. Soc., London, Sect A. **65**, 349–354 (1952)

41. Bedjaoui, A., Bouhemadou, A., Bin-Omran, S.: Structural, elastic and thermodynamic properties of tetragonal and orthorhombic polymorphs of Sr_2GeN_2: an ab initio investigation. High Pressure Research. **36**, 198–219 (2016)

42. Pugh, S.F.: Relations between the elastic moduli and the plastic properties of polycrystalline pure metals. Phil Mag. **45**, 823–843 (1954)

43. Anderson, O.L.: A simplified method for calculating the Debye temperature from elastic constants. J. Phys. Chem. Solids. **24**, 909–917 (1963)

44. Ravindran, P., Fast, L., Korzhavyi, P.A., Johansson, B.: Density functional theory for calculation of elastic properties of orthorhombic crystals: application to TiSi2. J Appl. Phys. **84**, 4891–4904 (1998)

45. Lloveras, P., Castán, T., Porta, M., Planes, A., Saxena, A.: Influence of elastic anisotropy on structural nanoscale textures. Phys. Rev. Lett. **100**, 165707–165704 (2008)

46. Ranganathan, S.I., Ostoja-Starzewski, M.: Universal elastic anisotropy index. Phys. Rev. Lett. **101**, 055504–055504 (2008)

47. Nye, J.F.: Properties of crystals. Oxford University Press, Oxford (1985)

48. Souadia, Z., Bouhemadou, A., Bin-Omran, S., Khenata, R., Al-Douri, Y., Al Essa, S.: Electronic structure and optical properties of the dialkali metal monotelluride compounds: Ab initio study. J. Mol. Graph. Model. **90**, 77–86 (2019)

49. Zou, D.F., Xie, S.H., Liu, Y.Y., Lin, J.G., Li, J.Y.: Electronic structure and thermoelectric properties of half-Heusler $Zr_{0.5}Hf_{0.5}NiSn$ by first-principles calculations. J. Appl. Phys. **113**, 193705–193707 (2013)